

---

# Chapter III

## Modification of Biodegradable Polymeric Matrices by Irradiation with MeV Ions

---

- 3.1 INTRODUCTION
- 3.2 RESULTS AND DISCUSSION
  - 3.2.1 *XRD Analysis*
  - 3.2.2 *FTIR Analysis*
  - 3.2.3 *Optical Analysis*
  - 3.2.4 *AC Electrical Frequency Response*
  - 3.2.5 *SEM Analysis*
- 3.3 CONCLUSIONS
- REFERENCES

---

Papers published in peer-reviewed journals related to this chapter:

1. Effects of MeV ions on physicochemical and dielectric properties of chitosan/PEO polymeric blend  
**Gnansagar B. Patel**, N.L. Singh, F. Singh, P.K. Kulriya  
Nucl. Instruments Methods Phys. Res. Sect. B Beam Interact. with Mater. Atoms. 447 (2019) 68–78.  
doi:[10.1016/j.nimb.2019.03.052](https://doi.org/10.1016/j.nimb.2019.03.052)
2. Effect of swift heavy ions irradiation on physicochemical and dielectric properties of chitosan and chitosan-Ag nanocomposites  
**Gnansagar B. Patel**, N.L. Singh, F. Singh, P.K. Kulriya  
Radiat. Phys. Chem. 181 (2021) 109288.  
doi:[10.1016/j.radphyschem.2020.109288](https://doi.org/10.1016/j.radphyschem.2020.109288)

# Chapter III

## Modification of Biodegradable Polymeric Matrices by Irradiation with MeV Ions

### 3.1 Introduction

The modification of biodegradable matrices is of inordinate interest to research communities as well as indigenous people due to versatile Eco-friendly physiognomies. This chapter bestows genuine chitosan and its physically modified matrix *via* blending with PEO, namely, CP blend. Since the chitosan matrices subjected to non-ionizing as well as ionizing radiation. However, exposed with proton beam, and heavier ions with energy in keV range are available in literature. The contextual of the CP blend is known to merely reconnoitre the UV treatments. So being curious to concede both these matrices concerning MeV ions exposure and successive responses, explicitly, structural, optical, morphological, and dielectric have discoursed in the current chapter. The synthesis approach, SHIs irradiation procedure, and relevance characterizations techniques were explained in details in the section 2.2., 2.3, and 2.4 of Chapter 2, respectively.

### 3.2 Results and Discussion

#### 3.2.1 XRD Analysis

XRD graphics for pristine chitosan and CP blend matrices are depicted in [Figure 3.1](#). The peaks at 2-theta values of 8.2°, 11.6°, 15°, 18°, and 21.7° are attributed to the characteristic diffraction pattern of chitosan structure [1]. The peaks evolved due to crystalline hydrate and anhydrous structure of chitosan are indorsed to 8.2° and 11.6° along with 15° respectively [2]. Indeed, the hydrated form of chitosan has bonded and also involved linkages of water molecules across the chains of chitosan might stabilizing the hydrated crystalline form [3]. Whereas, the peaks at 18°, and 21.7° ascribed to the amorphous feature [2]. The blend of chitosan with PEO polymer,

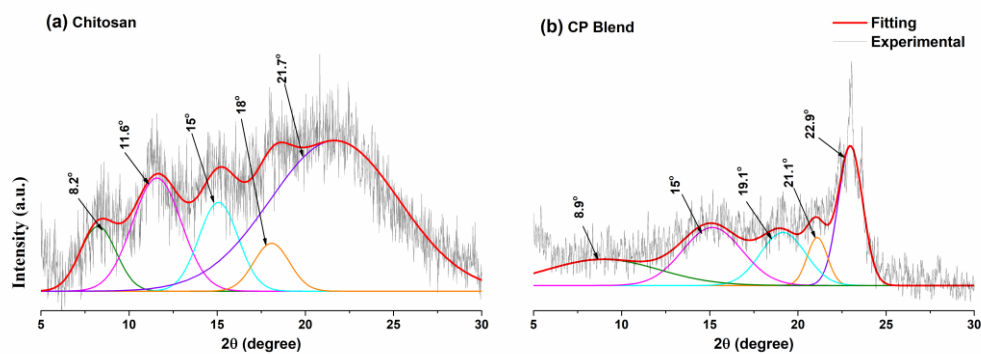


**Figure 3.1** XRD of (a) chitosan and (b) CP blend matrices

two distinctive peaks at 2-theta values  $19.1^\circ$  and  $22.9^\circ$  along with pre-existed diffraction patterns with minor shifting. Indicating that the blend of chitosan with crystalline PEO with 50:50 wt% of respective dried polymers revealed feeble or lack of interactions between the constituents. However, the chitosan itself acts as a plasticizer, and hence chitosan existence with PEO adeptly regulates the crystallization of PEO. So, the segmental and orientational mobility of polymeric main chains along with side chains significantly influenced, which can functionalized the soft, flexible and self-standing biodegradable matrix. The deconvolution approach has been used in order to distinguish the distinct diffraction peak as observed in [Figure 3.1](#). As an effects of SHIs, the structural features of biodegradable matrices are substantially reformed as noticed from the diffraction graphics that the peaks broadening moderately enhanced. As inferred in Chapter 2 (section 2.4.1), the crystallite size ( $L$ ) was calculated using Scherrer's methodology and tabulated in [Table 3.1](#). As already argued that the weak interaction between polymers yielding smaller crystallite size of CP blend than the chitosan as well as reasonably depends on blend ratio [4]. However, the change in the crystalline size of CP matrix in comparison with pristine chitosan revealed that the presence of PEO in CP matrix sustain its crystallite size upon radiation.

**Table 3.1** Variation in crystallite size of pristine and irradiated CS and CP blend matrices with 60-MeV  $C^{+5}$  and 100- MeV  $Ni^{+7}$  ions at the fluence of  $1 \times 10^{11}$  and  $1 \times 10^{12}$  ions/cm<sup>2</sup>

Fluence	Crystallite Size (Å)	
	Chitosan	CP Blend
Pristine	110.7	48.45
$C^{+5}$ ( $1 \times 10^{11}$ ions/cm <sup>2</sup> )	84.9	48.25
$C^{+5}$ ( $1 \times 10^{12}$ ions /cm <sup>2</sup> )	29.7	43.27
$Ni^{+7}$ ( $1 \times 10^{11}$ ions /cm <sup>2</sup> )	60.8	45.25
$Ni^{+7}$ ( $1 \times 10^{12}$ ions /cm <sup>2</sup> )	26.6	41.03

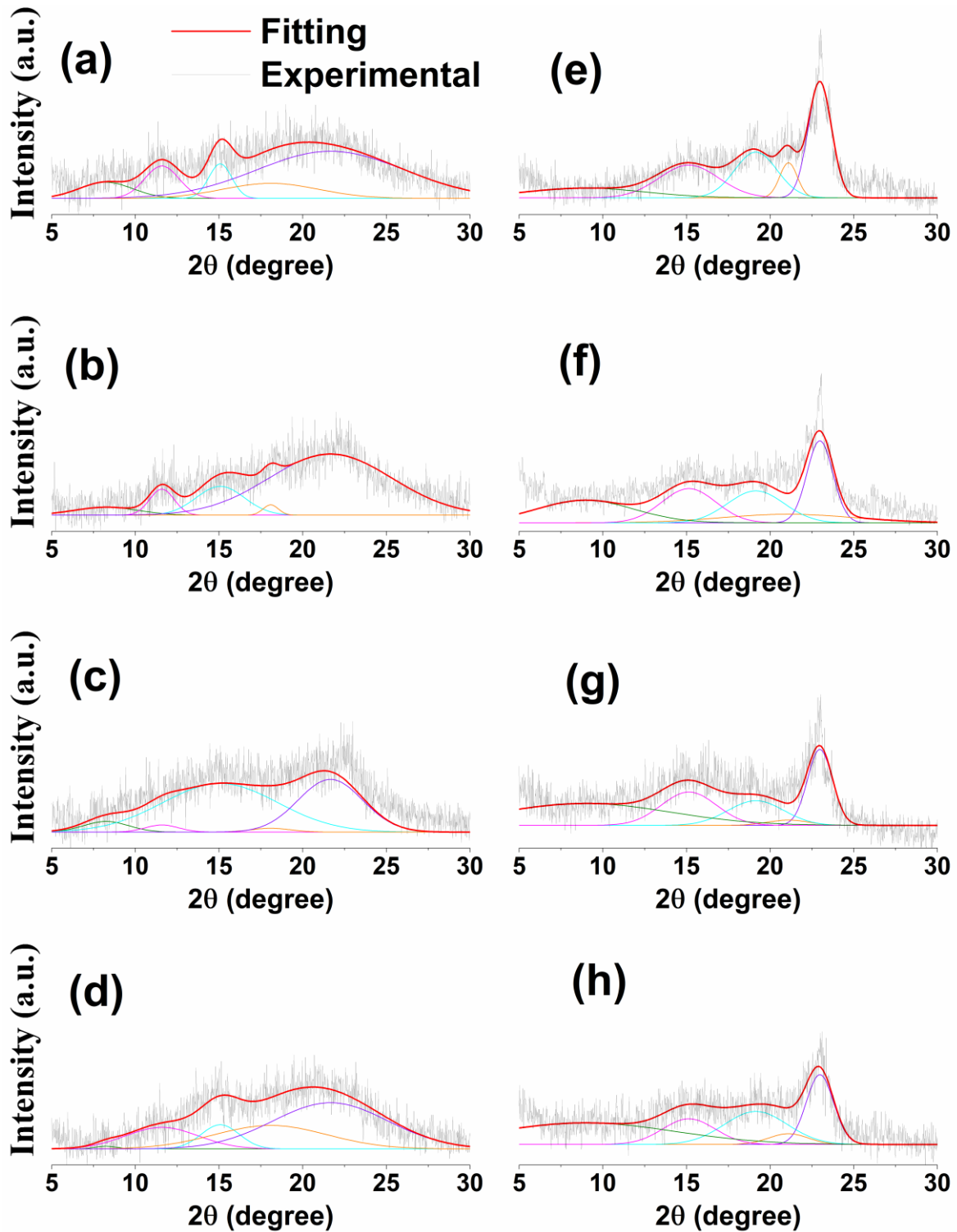


Figure 3.2 (a-d) XRD of chitosan irradiated with  $C^{+5}$  ions at the fluence of  $1 \times 10^{11}$  ions/cm<sup>2</sup>,  $1 \times 10^{12}$  ions/cm<sup>2</sup> and  $Ni^{+7}$  ions at the fluence of  $1 \times 10^{11}$  ions/cm<sup>2</sup>,  $1 \times 10^{12}$  ions/cm<sup>2</sup> respectively; (e-h) XRD of CP blend irradiated with  $C^{+5}$  ions at the fluence of  $1 \times 10^{11}$  ions/cm<sup>2</sup>,  $1 \times 10^{12}$  ions/cm<sup>2</sup> and  $Ni^{+7}$  ions at the fluence of  $1 \times 10^{11}$  ions/cm<sup>2</sup>,  $1 \times 10^{12}$  ions/cm<sup>2</sup> respectively.

Upon SHIs irradiation, the transient molten zones formed due to random ions cascade within the matrix destroy the delicate hydrogen linkages through which water molecules form bridge network with chitosan vital groups  $-NH$  or  $-OH$  yielding matrix with lack of water molecules. The deficiency of water molecule enhances the polymeric free volume influence the relaxation mechanisms, which could be revealed from [Figure 3.2](#), that the crystalline hydrate and anhydrous chitosan structure along with broader amorphous diffraction graphics, that is, FWHM increased with decreased intensity. In the case of CP blend, a similar trend observed upon SHIs irradiation, except, the crystalline diffraction pattern of PEO appeared at 2-theta value  $22.9^\circ$  moderately influenced. These results showed randomization *via* reorientation of macromolecule chains afterward the thermal equilibrium within formed transient molten zones. Moreover, perceived outcomes also endorse to enhance the free volume of biodegradable matrices at nanoscale extent.

### 3.2.2 ATR-FTIR Analysis

[Figure 3.3\(a\)](#) and [Figure 3.3\(b\)](#) depict the elementary vibrational bands of chitosan and CP Blend, respectively, in ATR-FTIR mode within the mid-infrared region as discussed in Chapter 2 (section 2.4.2). As revealed from [Figure 3.3\(a\)](#), the amide I mode of vibration evolved at  $1639\text{ cm}^{-1}$  ( $C=O$  stretching vibrations), while amide II at  $1540\text{ cm}^{-1}$  ( $-NH_3^+$ ) instead of  $1590\text{ cm}^{-1}$  ( $-NH_2$ ) confirmed the acetate nature of chitosan. As seen in  $3000\text{-}3600\text{ cm}^{-1}$  range, there exist extensive modes of vibration indorsed to hydrogen bonded O-H and N-H groups together with the interaction of O-H/N-H modes with  $C=O$  group of chitosan [4]. Chitosan also exhibits vibrational peaks at  $1149$  and  $1070\text{ cm}^{-1}$  (glucose rings) with  $1008\text{ cm}^{-1}$  (glycosidic linkage) and  $1258\text{ cm}^{-1}$  ( $-OH$ ). The modes also arising at  $1340\text{ cm}^{-1}$  ( $CH_2$  wagging),  $1445\text{ cm}^{-1}$  ( $CH_2$  scissoring),  $1410\text{ cm}^{-1}$  ( $CH_2$  bending and  $CH_3$  deformation),  $1377\text{ cm}^{-1}$  (symmetric  $CH_3$  deformation and CH bending),  $2907\text{ cm}^{-1}$  (symmetric C-H stretching), and  $2962\text{ cm}^{-1}$  (asymmetric C-H stretching) [5].

Briefly, the vibrational mode from PEO evolving at  $1060\text{ cm}^{-1}$  ( $C-O-C$  stretching),  $842\text{ cm}^{-1}$  ( $CH_2$  rocking),  $1341\text{ cm}^{-1}$  and  $1360\text{ cm}^{-1}$  ( $CH_2$  wagging),  $1447\text{ cm}^{-1}$  and  $1465\text{ cm}^{-1}$  ( $CH_2$  scissoring),  $1412\text{ cm}^{-1}$  ( $CH_2$  bending and  $CH_3$  deformation),  $2877\text{ cm}^{-1}$ ,  $2928\text{ cm}^{-1}$ , and  $2962\text{ cm}^{-1}$  (CH stretching) are perceived in the spectrum of CP blend, as seen in [Figure 3.3\(b\)](#). Upon blending PEO with chitosan, vibration modes arising from chitosan and PEO both co-existed

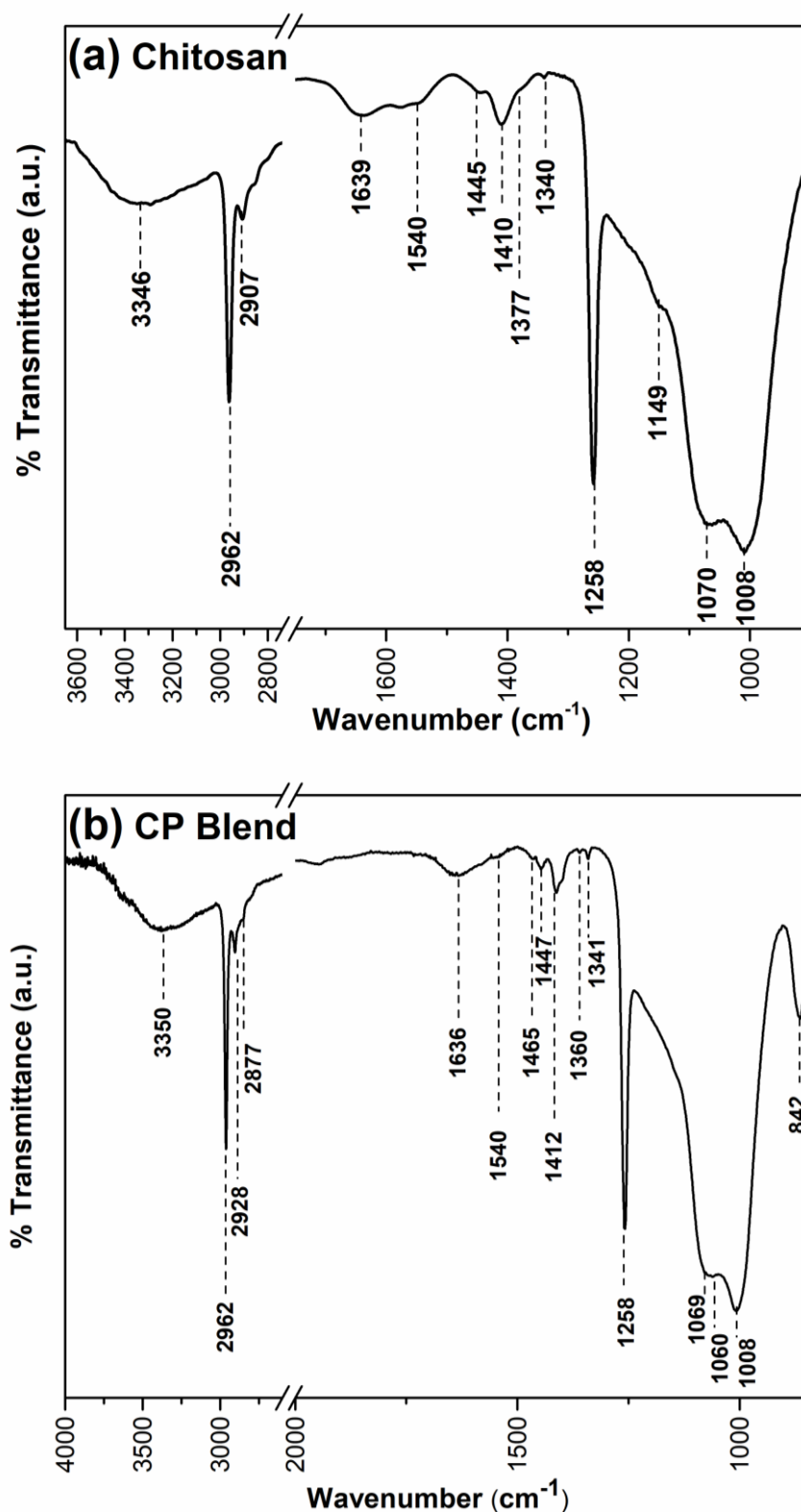


**Figure 3.3 FTIR spectra of (a) chitosan and (b) CP blend**

with minor shift as revealed from [Figure 3.3\(b\)](#) indorsed to feeble macromolecules interactions, mainly at the interphase of constituting polymers. These results well collaborated with XRD.

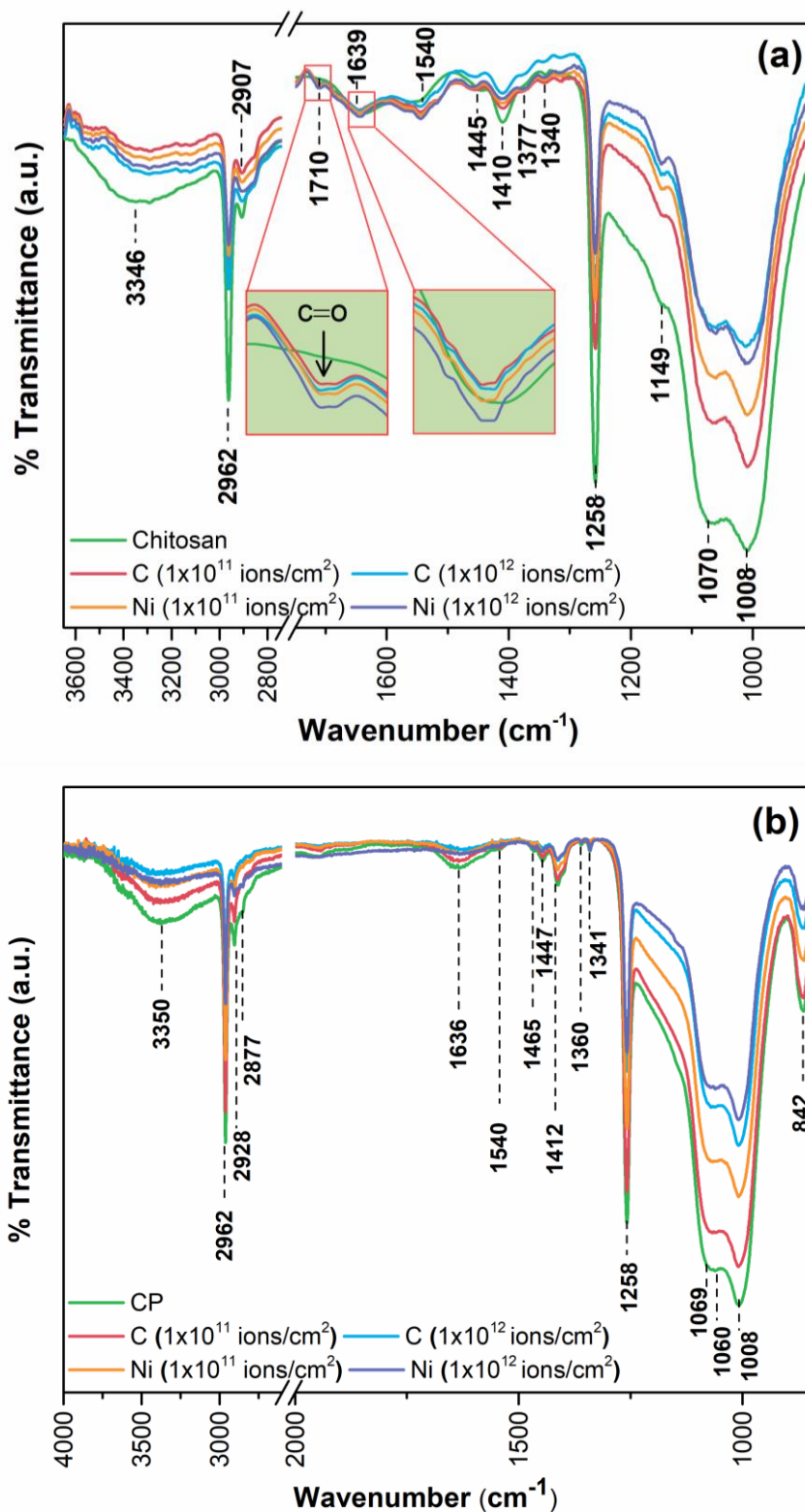


**Figure 3.4** FTIR spectra of (a) chitosan and (b) CP blend irradiated with C<sup>+5</sup> and Ni<sup>+7</sup> ions at the fluence of 1×10<sup>11</sup> ions/cm<sup>2</sup> and 1×10<sup>12</sup> ions/cm<sup>2</sup> respectively

At first, the noteworthy impact of C<sup>+5</sup> and Ni<sup>+7</sup> ions irradiation on vibrational modes of chitosan perceived from Figure 3.4(a). The evolved newer mode of vibration at 1710 cm<sup>-1</sup>

attributed to carbonyl bond (C=O) vibrations as appeared and shown in the inset of Figure 3.4(a). The relocation to the higher wavenumber of amide I (See inset of Figure 3.4) ascribed to the branching of intra-chain hydrogen network established between molecules of water and representative -OH and -NH<sub>2</sub> of chitosan, which facilitates removal of the adsorbed water. The rupture of glycidyl bonds present in C-O-C groups linking tetrahydropyran rings could perceive from the diminishing intensity of bonds 1149 and 1070 cm<sup>-1</sup>. The overlapped stretching of O-H and N-H observed at 3346 cm<sup>-1</sup> is significantly detracted upon SHIs irradiation although it does not utterly vanish. The -OH bending mode appeared at 1258 cm<sup>-1</sup> is moderated without peak widening. The momentous hydrogen abstraction yielding decreased in rational H/C value, which could be inferred from substantial suppression of various modes, explicitly, arising at 1340 cm<sup>-1</sup>, 1377 cm<sup>-1</sup>, 1410 cm<sup>-1</sup>, 1445 cm<sup>-1</sup>. The waning of symmetric C-H stretching modes is minor in comparison with asymmetric C-H stretching modes observed at 2907 cm<sup>-1</sup> and 2962 cm<sup>-1</sup> respectively.

In the case of CP blend, SHIs induced impact on macromolecular structural characteristics are also depicted in Figure 3.4(b). The presence of PEO in the CP matrix hindered the carbonyl group formation upon irradiation. Conversely, the formation of the carbonyl bond is originated in the case of chitosan as found in spectra. This reveals a mutual stabilizing effect as a consequence of the simultaneous involvement of constitutional elements of both polymers during the irradiation process. Indeed, the crystalline phase of PEO exhibited resistant to SHIs irradiation in comparison with chitosan and hence can hinder the overall degradation of the CP blend. These arguments are supported by XRD analysis. However, as discussed in Chapter 2 (section 2.3.3), the values of  $S_e$  of C<sup>+5</sup> and Ni<sup>+7</sup> ions of the order of keV, which is reasonably superior to the threshold energy (few eV/Å) of the polymeric matrix. These results in massive rupture of polymeric linkages as a consequence of origination of transient molten latent track along the ion trajectory or creation of columnar type defect in polymer matrix [6]. Hence, the intensities of vibration modes of CP blend perceived to be diminished with a trivial shift upon irradiation.

Inclusively, as an effect of SHIs on polymeric matrices, the low molecular weight ions and radicals are formed and there is a probability of escaping from the host matrix due to shielded with high vacuum or eternally become a part of the bulk. Moreover, SHIs cause randomization of macromolecular chains, that is, branching of the main chains and macromolecular structure

degradation occurred at backbones and side-chains *via* mainly extrication of hydrogen and carbon [7]. Therefore, the physical characteristics and the chemical structure of the polymeric matrix are highly influenced.

### 3.2.3 Optical Analysis

Chitosan and CP blend have immense relevance in cosmetics, pharmacy, medicine, and optoelectronic applications [8] owing to the advantages of biodegradability, biocompatibility, and non-toxic features, therefore, it becomes necessitate to study the optical responses of such matrices as a function SHIs parameters. To avail the relative chance in UV-visible absorption responses of pre and post irradiated chitosan and CP blend, their spectra are collectively illustrated in Figure 3.5. The absorption peak at 310 nm exhibited relatively greater intensity in the case of chitosan is moderated upon blending with PEO. The existence absorption peak for both chitosan and CP blend spectra is attributed to the acetate form of matrices, which is also aforesaid in FTIR analysis. Additionally, the graphics of both matrices in the visible range (~400–800 nm) show minor absorption indorsed to the entirely bound nature of the electrons [9] in the biodegradable matrices.

In pursuit of SHIs irradiation, there is a boost in absorption intensity within a span of the UV with an increase in fluence. The differential absorbance ( $A-A_0$ ) at 370 nm wavelength appreciably intensified as shown in the inset graph of Figure 3.5. The efficient UV photon absorption in the wavelength region less than 370 nm point out the utilization of such matrices for shielding UV light. Remarkably enhanced absorption of the prevailing peak at 310 nm ascribed to establishing color responsive resonating matrix owing to the creation of distinctive conjugated linkages, explicitly, C=O, C=C and C=NH, etc. [10]. Hence, the existence of such chromophores within the matrix yielded color transformation of biodegradable matrices from pale yellow to dark yellow, brown, and dark brown with increasing fluence (images not illustrated here). Reform in absorption edge shape also noticed with persisted red shift as the ion fluence increased. These results facilitate selectively  $n \rightarrow \pi^*$  and  $\pi \rightarrow \pi^*$  electron transition, which influenced the optical energy bandgap of biodegradable matrix and estimated using Tauc's approach as discussed in chapter 2 (section 2.4.3).

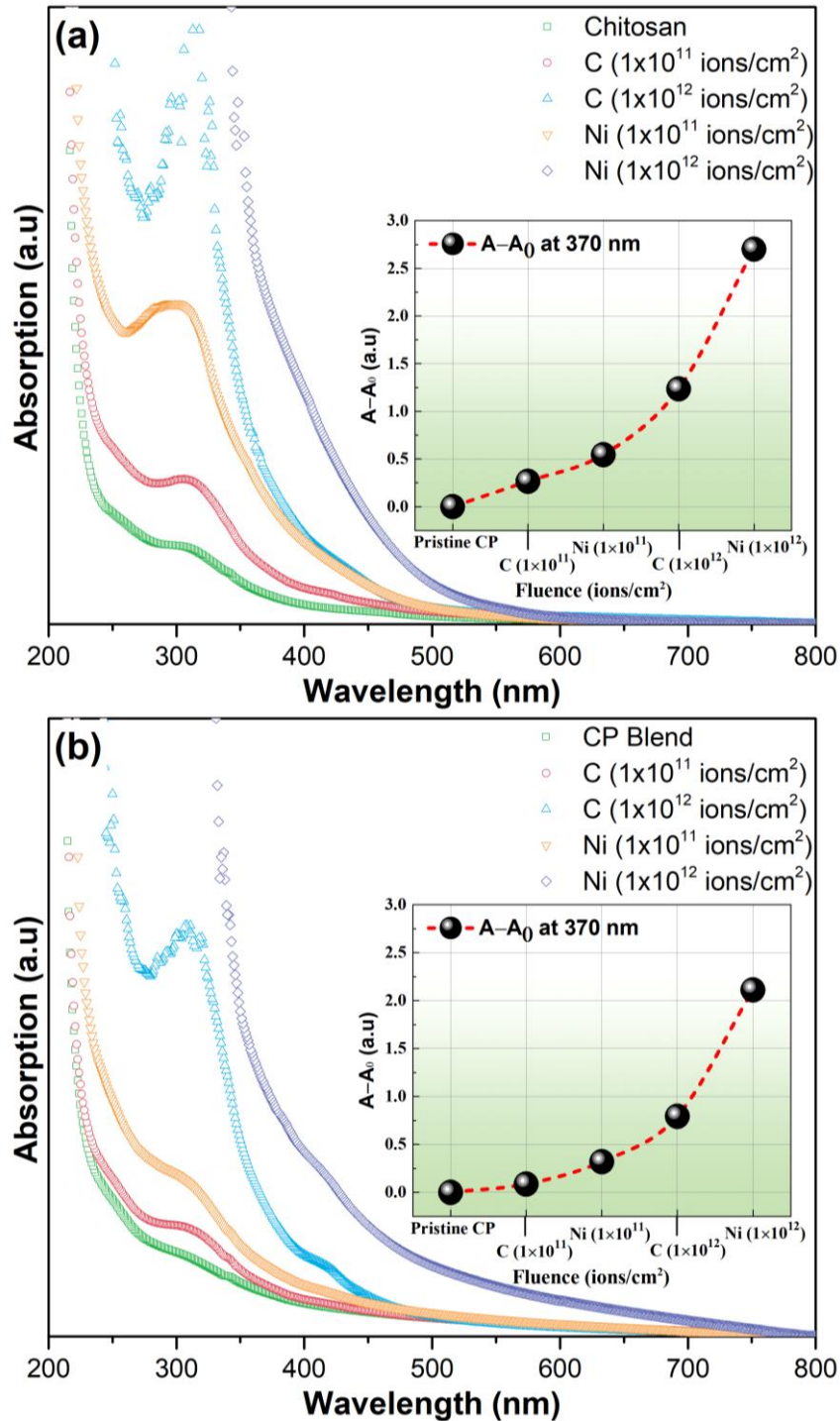


**Figure 3.5** UV-Visible absorption spectra of (a) chitosan and (b) CP blend irradiated with C<sup>+5</sup> and Ni<sup>+7</sup> ions at the fluence of  $1 \times 10^{11}$  ions/cm<sup>2</sup> and  $1 \times 10^{12}$  ions/cm<sup>2</sup> respectively

Figure 3.6 depicts the Tauc's plot of pre and post C<sup>+5</sup> and Ni<sup>+7</sup> ions irradiated chitosan and CP blend. The graphics are subjected to linear least square statistics yielding  $E_g$  with S.D. and goodness-of-fit ( $R^2$ ) for respective matrix tabulated in Table 3.2. The accuracy of estimations showed better reliability that can be inferred from marking  $R^2$  values closer to unity. Upon C<sup>+5</sup> ions irradiation, the  $E_g$  for chitosan and CP blend decreased by  $\sim 39\%$  and  $\sim 27\%$ , respectively.

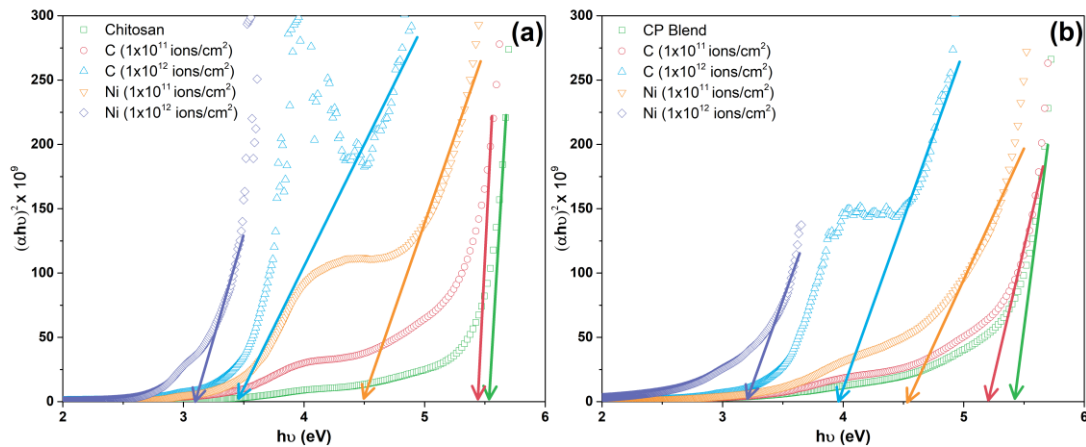


**Figure 3.6** Tauc's plots of (a) chitosan and (b) CP blend irradiated with  $C^{+5}$  and  $Ni^{+7}$  ions at the fluence of  $1 \times 10^{11}$  and  $1 \times 10^{12}$  ions/cm<sup>2</sup>, respectively.

Whereas upon  $Ni^{+7}$  ions irradiation corresponding value declined by  $\sim 45\%$  and  $\sim 40\%$ , respectively. Hence, heavier  $Ni^{+7}$  with greater energy and mass cause to a prompt decrease in bandgap, particularly, in the case of chitosan matrix than the other one. The successive decreased in  $E_g$  with increased fluence endorse the prolonged defects at band edge towered the forbidden band and/or there may originate the intermediate energy level in the forbidden gap [1,11]. Another promising reason is the enrichment of localized charge carrier density due to the randomization of macromolecular restructurings with the outgassing of volatile gases [1,11].

**Table 3.2** Variation in  $E_g$ ,  $N$ , and  $R^2$  for (a) chitosan and (b) CP blend irradiated with  $C^{+5}$  and  $Ni^{+7}$  ions at the fluence of  $1 \times 10^{11}$  and  $1 \times 10^{12}$  ions/cm<sup>2</sup>, respectively.

Fluence	Chitosan			CP Blend		
	$E_g$ (eV)	$R^2$	$N$	$E_g$ (eV)	$R^2$	$N$
Pristine	$5.64 \pm 0.02$	0.97	-	$5.40 \pm 0.01$	0.97	-
$C^{+5}$ ( $1 \times 10^{11}$ ions/cm <sup>2</sup> )	$5.49 \pm 0.02$	0.91	39	$5.19 \pm 0.02$	0.95	44
$C^{+5}$ ( $1 \times 10^{12}$ ions /cm <sup>2</sup> )	$3.44 \pm 0.01$	0.98	100	$3.92 \pm 0.04$	0.93	77
$Ni^{+7}$ ( $1 \times 10^{11}$ ions/cm <sup>2</sup> )	$4.96 \pm 0.02$	0.97	48	$4.54 \pm 0.03$	0.96	57
$Ni^{+7}$ ( $1 \times 10^{12}$ ions /cm <sup>2</sup> )	$3.10 \pm 0.01$	0.96	122	$3.23 \pm 0.02$	0.95	113

Besides, a prominently decrease in H/C ratio facilitates  $sp^2$  hybridization, consequently, yielded clustering of hydrogenated amorphous carbon within the matrix. As discussed in Chapter 2 (section 2.4.3), the amended approach of Fink *at al.* employed for an estimate of the number of carbon atoms per conjugation length ( $N$ ) and listed in Table 3.2. The carbon atoms structure condensed in case of  $Ni^{+7}$  ions induced clustering is excess than  $C^{+5}$  ions irradiation

attributed to higher  $S_e$  value of  $\text{Ni}^{+7}$  ion. The localized foundation of carbon clusters might consecutively reflected in dielectric relaxation and conduction phenomenon owing to acquired *carbon-rich* biodegradable matrices. It is worthy to note that the size of the compact cluster immensely frequency dependant. Indeed, the thermal quenching upon ions irradiation gets overlapped with an increase in fluence due to successive transient events in a pretty short era [6].

### 3.2.4 AC Electrical Frequency Response

The biodegradable polymeric matrices investigated in broad dielectric spectroscopy as a function of frequency mainly concerning distinctive localized polarizations viz. electrode, interfacial, orientation, electronic, atomic [12]. The plots of dielectric constant ( $\epsilon'$ ) vs. log frequency for pre and post  $\text{C}^{+5}$  and  $\text{Ni}^{+7}$  ions irradiated chitosan and CP blend are plotted in Figure 3.7. Ostensibly, the frequency-dependent response of pristine and radiation treated chitosan and CP blend exhibited alike graphical patterns with dispersive behavior in 20 Hz–3 kHz and 20 Hz–4 kHz frequency window, respectively. The values of  $\epsilon'$  at low-frequency domain achieved imperious response, whereas corresponding values at higher frequency domain attained relatively lower value. Indeed, the response in the lower frequency window indorsed origination of electrical double layer (i.e. space charge/interfacial polarization) at the interface of biodegradable matrices and electrode boundaries due to accumulation of charge carriers [12,13]. Indeed, the long-range charge carries migration and following response of permanent dipole moments, thanks to  $-\text{NH}_2$  and  $-\ddot{\text{O}}-$  groups to external oscillating field changed with a slower rate at the lower frequency. Beyond 3 kHz and 4 kHz for chitosan and CP blend matrices respectively, the observed flatten domain indorsed to short-range charge carrier drift as well as the segmental and side chains of macromolecules lags behind the field varying relatively faster at higher frequency window. It is observed that the  $\epsilon'$  values show reasonable dependency on the beam parameters. Increased  $\epsilon'$  values at low frequency indorsed to the branching of polymeric main and side chains with the formation of low molecular weight radicals. As a result, the post-irradiated matrices have enhanced charge carriers density

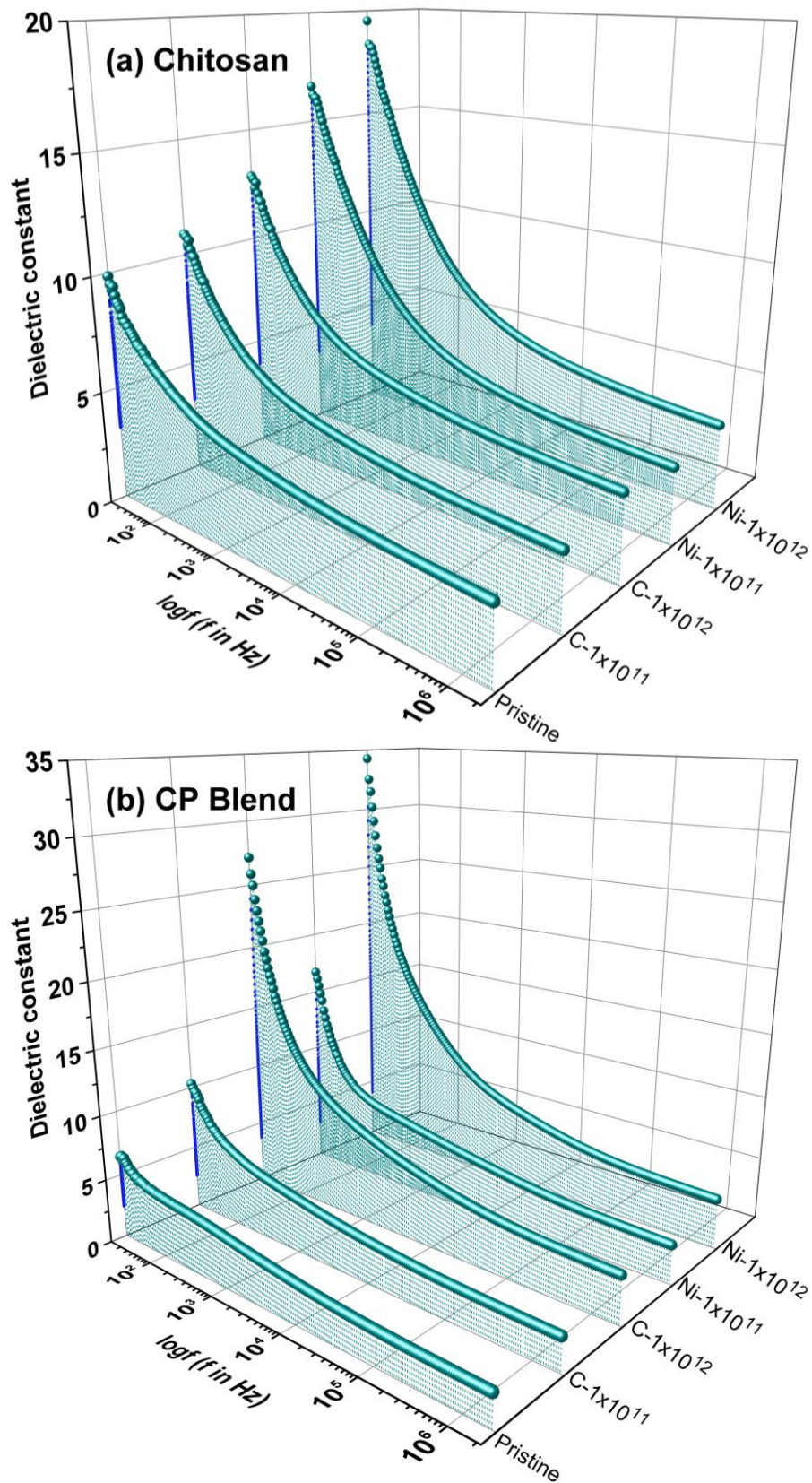


Figure 3.7 Plot of dielectric constant ( $\epsilon'$ ) versus log frequency for pre and post C<sup>+5</sup> and Ni<sup>+7</sup> ions irradiated (a) chitosan and (b) CP blend matrices

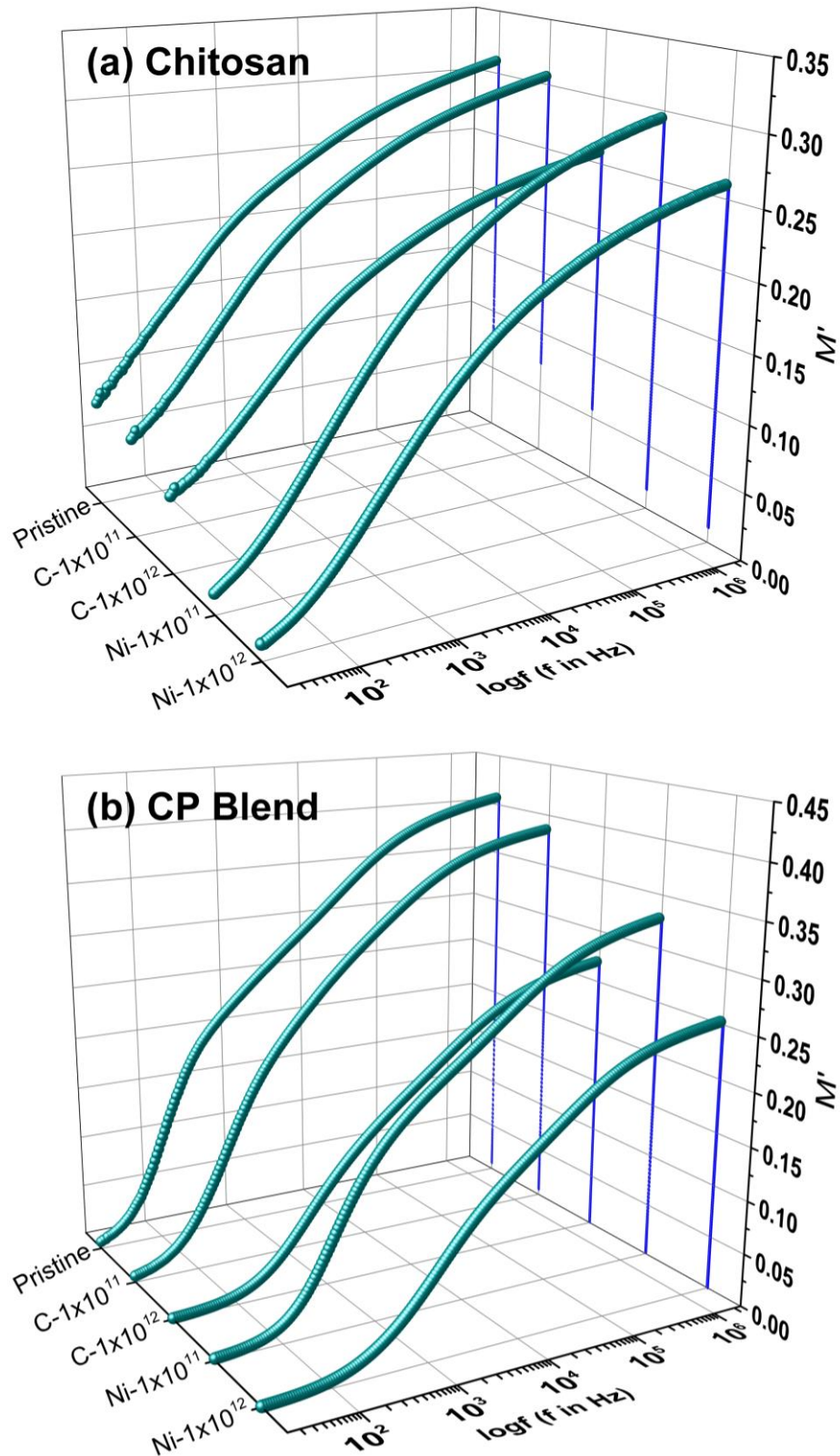


Figure 3.8 Plot of real electric modulus ( $M'$ ) versus log frequency for pre and post C<sup>+5</sup> and Ni<sup>+7</sup> ions irradiated (a) chitosan and (b) CP blend matrices

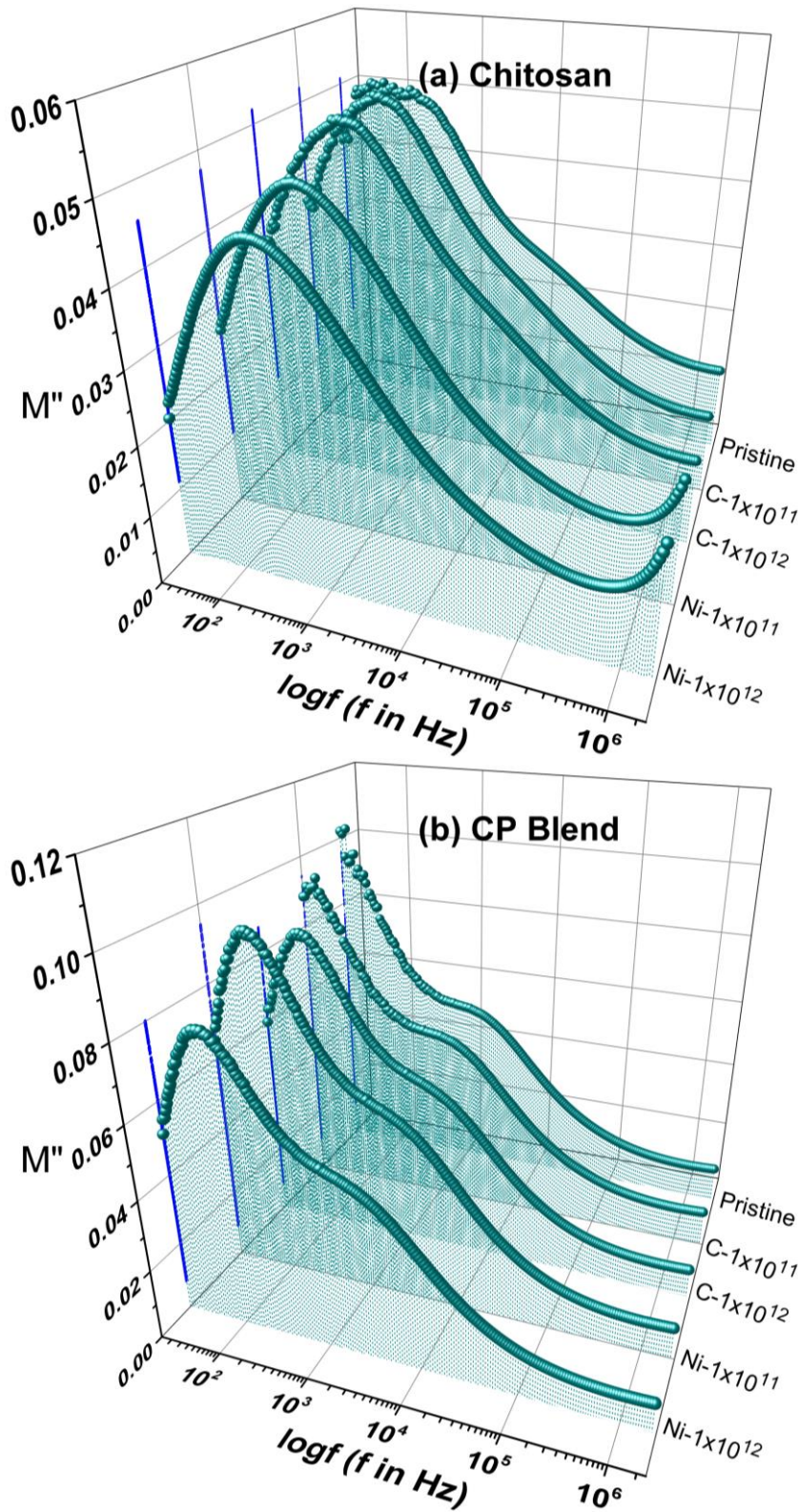


Figure 3.9 Plot of imaginary electric modulus ( $M''$ ) versus log frequency for pre and post  $C^{+5}$  and  $Ni^{+7}$  ions irradiated (a) chitosan and (b) CP blend matrices

revealed their effect at the high-frequency domain. Whereas there might decrease in moment of inertia of macromolecules due to branching of chains, which could easily follow the field and shows their attributes to low frequency.

An adequate implication of dielectric modulus formalism enables to insight and inspect the relaxation and conduction phenomenon by suppressing the low frequency instigation of space charge and interfacial polarization. As well, this formalism ceased the various provokes arising during the assessment, that is, electrical contact between electrode and specimen, physicochemical state of the electrode, absorbed impurities etc. [14]. The graphics of real electric modulus ( $M'$ ) vs. log frequency for  $C^{+5}$  and  $Ni^{+7}$  ions irradiated chitosan and CP blend are illustrated in Figure 3.8. The values of  $M'$  seems to be quite inferior ( $M' \rightarrow 0$ ) as a frequency approach to zero ( $f \rightarrow 0$ ) confirmed the ceases of space charge and interfacial polarization [15]. An asymptotic increase in  $M'$  with an increase in frequency and at higher frequencies perceived to be level off as  $M'$  attained the maximum value by virtue of dispersive conductivity relaxation [14,15]. Upon SHIs irradiation, the predominant decline in  $M'$  across the broad frequency range is observed. These results are attributed to ease of segmental, side chain, and charge carrier mobility to decrease in rigidity or moment of inertia of polymeric chains. Indeed, enhanced nanoscale free volume and randomization of polymeric matrices, as explained in XRD and IR responses, facilitated more room and chains with lower molecular weight presumably influence the localized macromolecular motion.

At a glance, a well-resolved peak in the graphics of imaginary electric modulus ( $M''$ ) vs. log frequency for both chitosan and CP blend is perceived from Figure 3.9. The  $M''$  plot of chitosan evolve a distinct solo peak. The  $M''$  spectra of CP blend as expected consists of two relaxation processes due to the coexistence of semi-crystalline and amorphous phases. The relaxation at lower frequency revealed the transformation of long-range motion to rotational or segmental motion of charge carriers, while the faster relaxation at higher frequency attributed to polar side group motion [16]. For both chitosan and CP blend exhibit a shift of relaxation peak toward higher frequency region. However, the relaxation peak appeared at a higher frequency in the spectra of the CP blend become wider with trivial shift. The influence of  $M''$  spectra upon SHIs irradiation evidence of structural reorganization and defect formation.

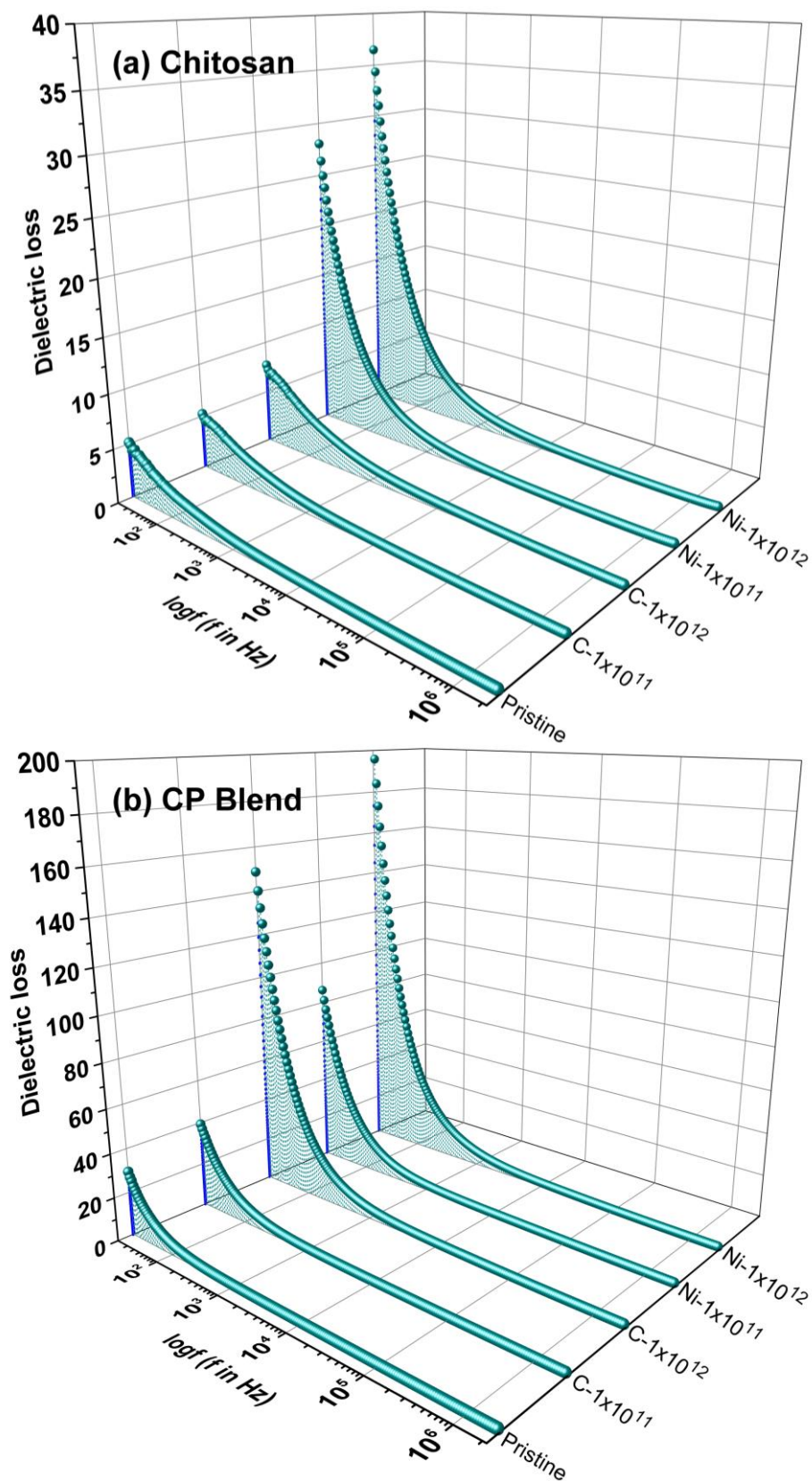
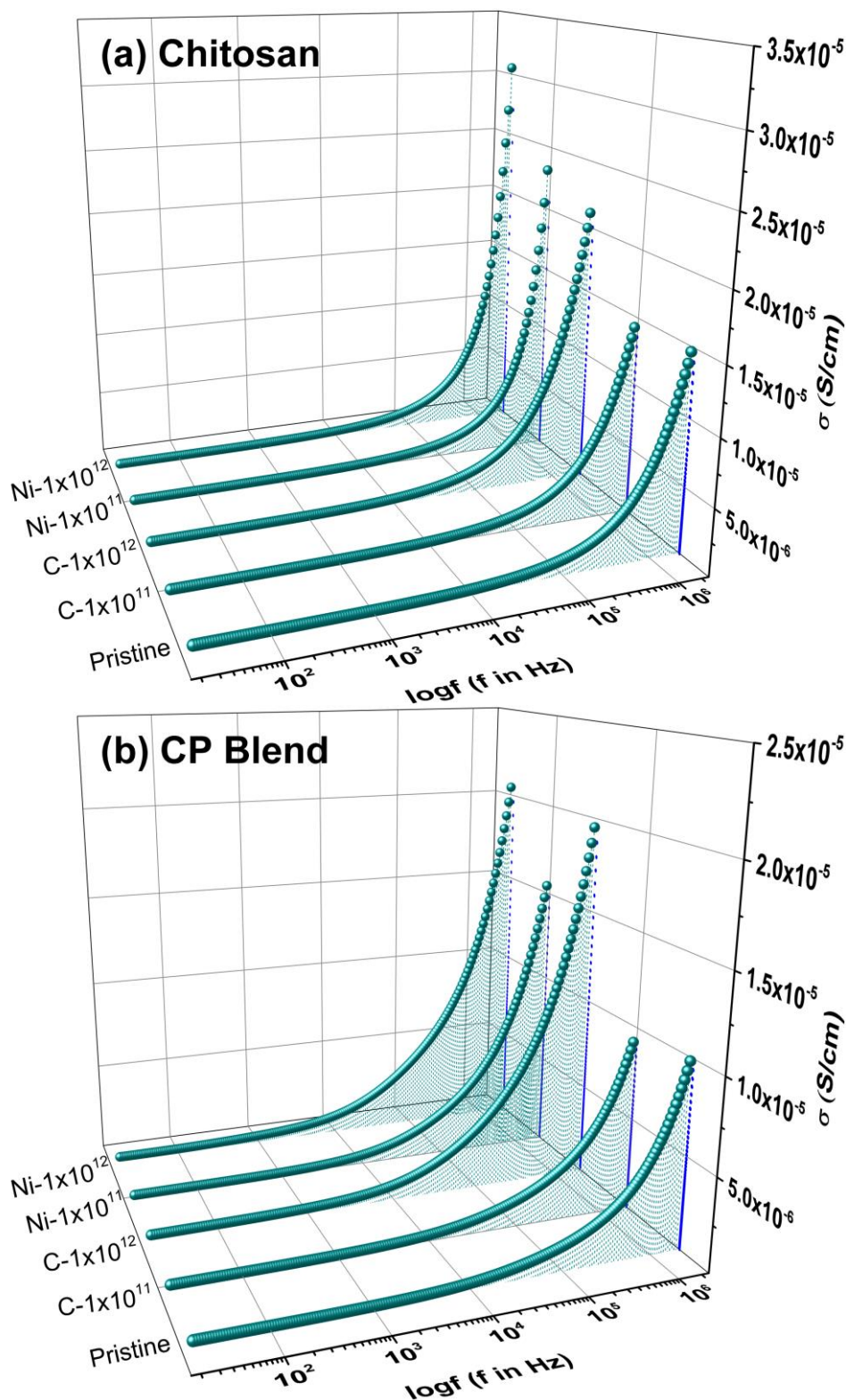


Figure 3.10 Plot of dielectric loss ( $\epsilon''$ ) versus log frequency for pre and post C<sup>+5</sup> and Ni<sup>+7</sup> ions irradiated (a) chitosan and (b) CP blend matrices



**Figure 3.11** Plot of conductivity ( $\sigma$ ) versus log frequency for pre and post C<sup>+5</sup> and Ni<sup>+7</sup> ions irradiated (a) chitosan and (b) CP blend matrices

The dielectric loss ( $\epsilon''$ ) spectra for chitosan and CP blend have been plotted in Figure 3.10. As perceived that there is no loss peak in both spectra and exponentially decreasing tendency with

an increase in frequency. The exponential dependency of  $\varepsilon''$  spectra for both matrices show prevailing polarization dominance than the dc conductivity [17]. Comparatively moderate loss is observed in the case of chitosan at a lower frequency domain than the CP blend. Also, the SHIs assisted collective drift of induced charge carriers in association with segmental relaxation process might be reflected in the phenomenon of charge carriers hopping.

Figure 3.11 illustrates the frequency-dependent conductivity spectra. The graphics show frequency independent plateau at lower frequency domain and exhibited dispersion at higher frequency accredited to  $\sigma_{dc}$  and  $\sigma_{ac}$  conductivity respectively. The matrices under investigation follow Jonscher universal power law [18]. Enhance in conductivity is figure out upon  $C^{+5}$  and  $Ni^{+7}$  ions irradiation. Applying the statistical evaluation as explained in Chapter 2 (section

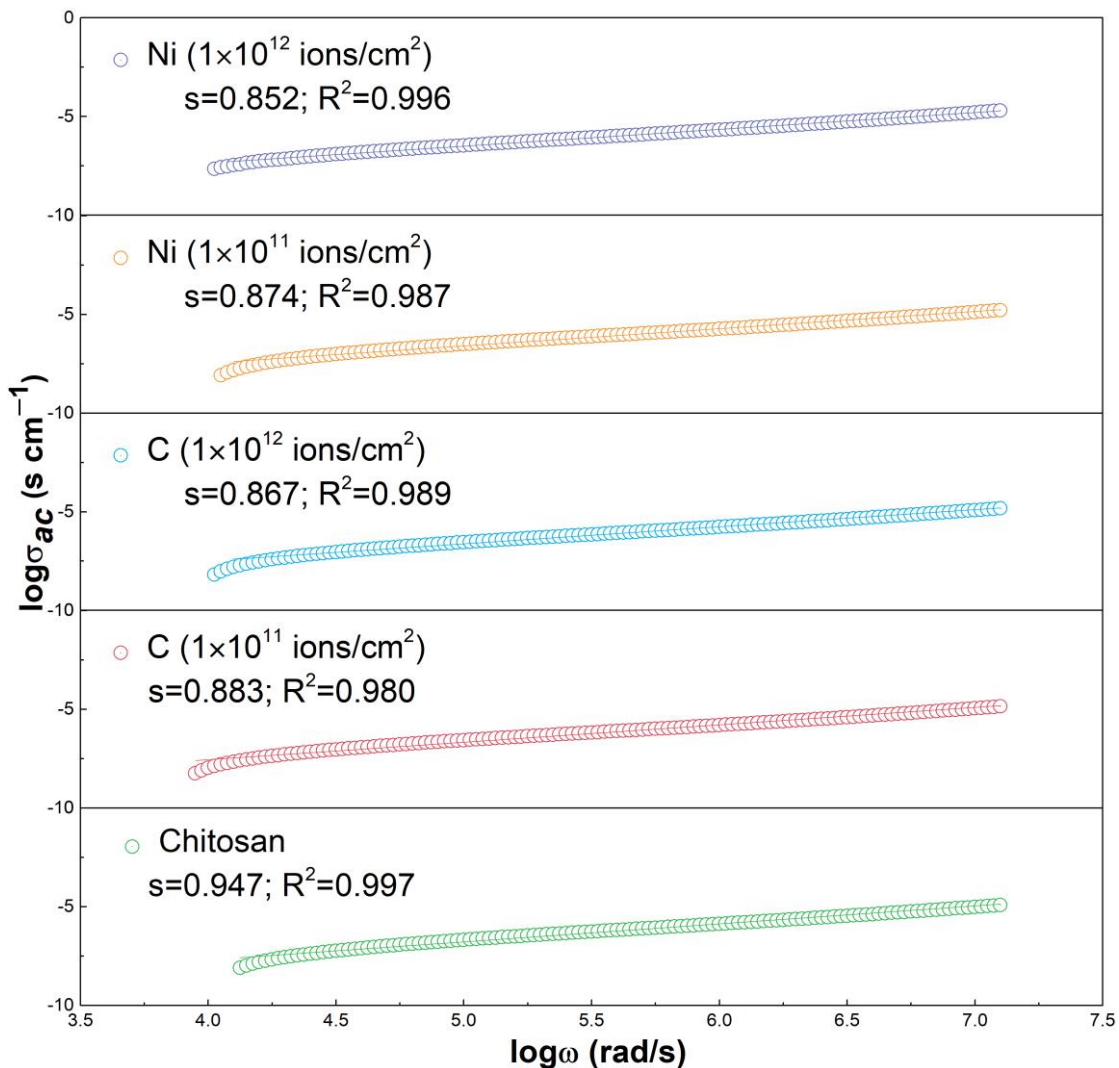


**Figure 3.12** Plot of log ac conductivity versus log angular frequency for pre and post  $C^{+5}$  and  $Ni^{+7}$  ions irradiated chitosan

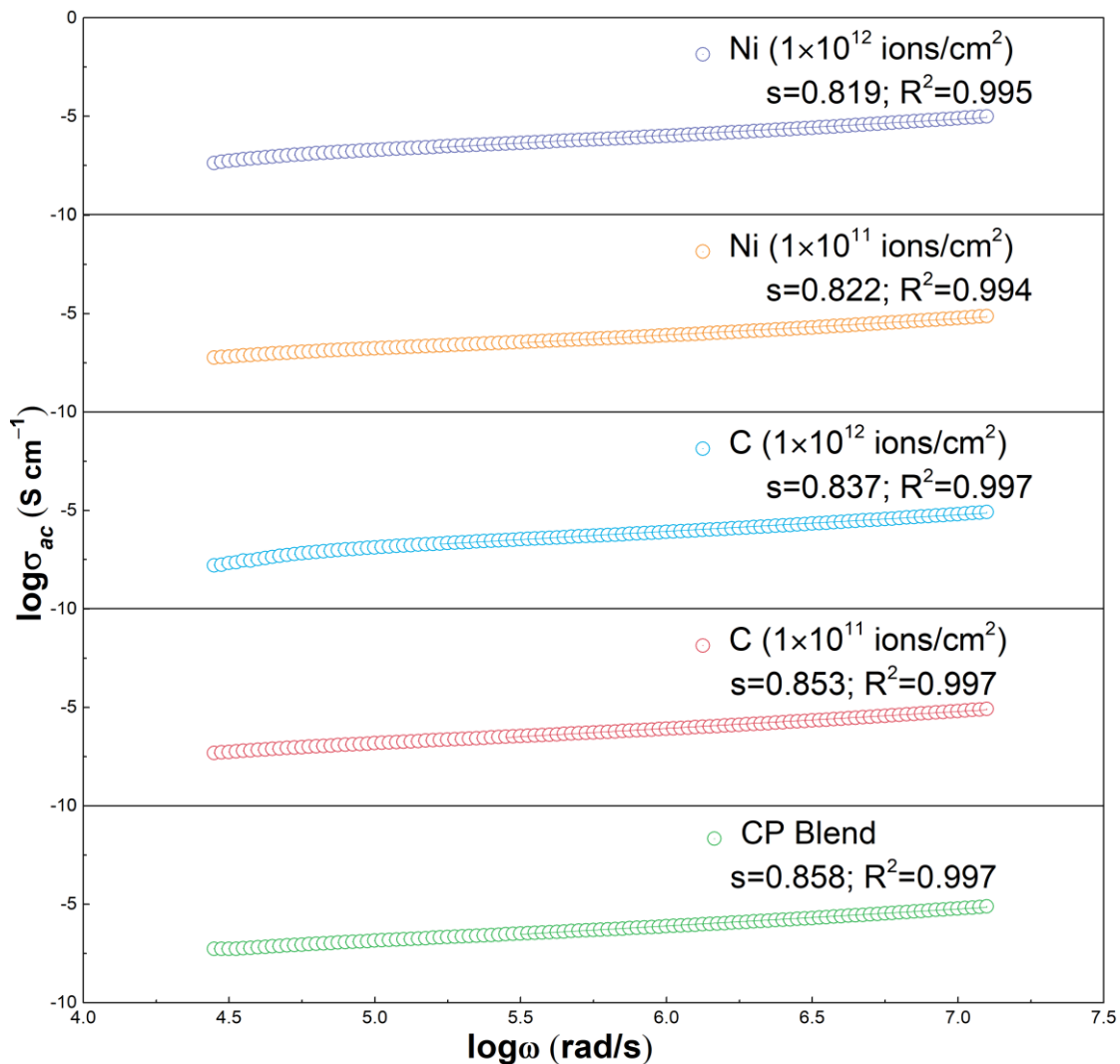


**Figure 3.13** Plot of  $\log ac$  conductivity versus  $\log$  angular frequency for pre and post  $C^{+5}$  and  $Ni^{+7}$  ions irradiated CP blend

2.4.4), the dc conductivity and the power exponent “s” measured and exhibited reasonable dependency on the fluence of respective ion. Upon  $C^{+5}$  ions irradiation, the  $\sigma_{dc}$  for chitosan and CP blend improved by  $\sim 142\%$  and  $\sim 165\%$ , respectively. While upon  $Ni^{+7}$  ions irradiation corresponding value amended by  $\sim 405\%$  and  $\sim 279\%$ , respectively. The value of “s” was calculated for chitosan and CP blend from  $\log\sigma_{ac} \rightarrow \log\omega$  graph and insert within the respective plot is shown in [Figure 3.12](#) and [Figure 3.13](#), respectively. For chitosan, “s” attained the value in between 0.94-0.85 and respective estimation for CP blend found between 0.86-0.82 with consistent fitting as  $R^2$  is nearer to unity. Therefore, the phenomenon of charge carriers hopping between adjacent sites of biodegradable macromolecule facilitates AC conduction [18]. The transition in  $\sigma_{ac}$  is accompanied by modifications upon a radiation treatment is evidence of the

formation of free radicals, randomization of polymeric chains,  $sp^2$  hybridization, and development of carbon-rich conductive network within the matrix as well as increasing an extent of amorphization and free volume [6,11,19].

### 3.2.5 SEM Analysis

Figure 3.14(a-f) exhibits FESEM images at scale values of 1  $\mu\text{m}$  and 200 nm (inset image) for pristine chitosan and CP blend and their  $\text{C}^{+5}$  and  $\text{Ni}^{+7}$  ions irradiated matrices at  $1 \times 10^{12}$  ions/ $\text{cm}^2$  fluence. The nodules seen from chitosan micrograph evolved crystallized domains molded due to slower evaporation rate yielding typically irregular morphology [20]. The presence of nodules resembles hydrated crystalline ( $8.2^\circ$  and  $11.6^\circ$ ) and anhydrous crystalline ( $15^\circ$ ) features of chitosan as explained in XRD. The tiny crevices as can perceive from the inset image indorsed to the chitosan semi-crystalline. Whereas, the SEM micrograph of the CP blend revealed substantially larger knots conceding highly distorted morphology validate the existence of lamellae assorted spherulites structure of PEO [21]. Indicating dominance of the crystalline nature of the CP blend as revealed in XRD. The nearby and adjacent regions concerning the knots are attributed to the amorphous phase [22]. The observed phase separation is evidence of weak interaction between two polymers, mainly at the interface as discussed in physicochemical responses. However, ease of macromolecular orientation governs by the degree of amorphous domain and is reflected in dielectric responses.

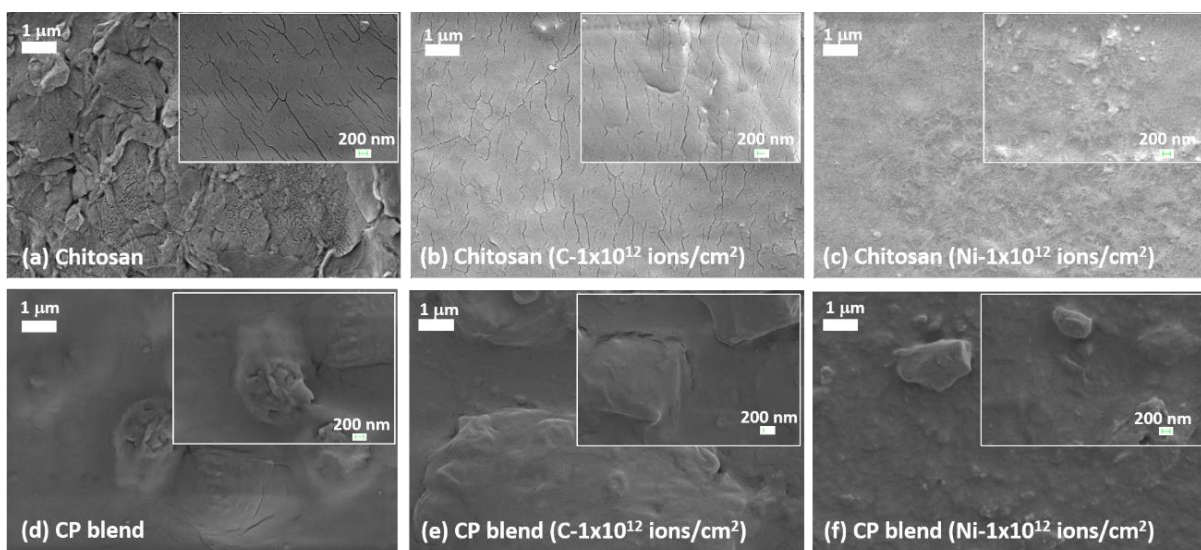


**Figure 3.14 SEM micrographs of chitosan (a) irradiated with  $\text{C}^{+5}$  (b) and  $\text{Ni}^{+7}$  (c) ions at the fluence of  $1 \times 10^{12}$  ions/ $\text{cm}^2$ ; CP blend (d) irradiated with  $\text{C}^{+5}$  (e) and  $\text{Ni}^{+7}$  (f) ions at the fluence of  $1 \times 10^{12}$  ions/ $\text{cm}^2$**

Upon  $C^{+5}$  and  $Ni^{+7}$  ions irradiation, the surface feature of both matrices substantially reformed. The surface becomes relatively flatter and smoother. The  $Ni^{+7}$  ions authentically cause greater impact due to relatively higher  $S_e$  value and heavier mass compared to  $C^{+5}$  ions. The suppression of nodules and knots upon SHIs irradiation transpired smoother surface is evidence of an increase in the amorphous phase.

### 3.3 Conclusions

Upon  $C^{+5}$  and  $Ni^{+7}$  ions irradiation with different fluences on biodegradable chitosan and CP blend matrices responded uniquely, which reflected in their physicochemical and dielectric

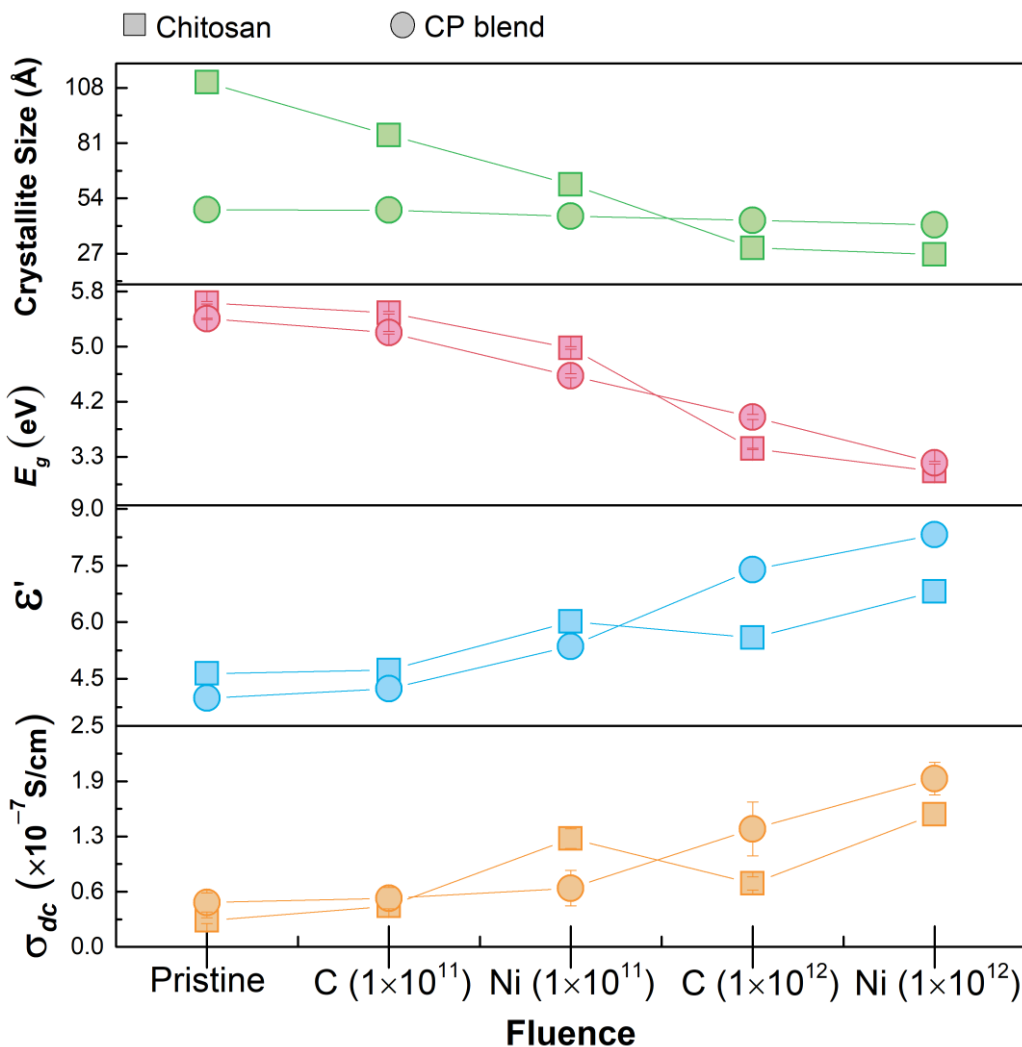


**Figure 3.15** Variation in crystallite size, bandgap ( $E_g$ ), dielectric constant ( $\epsilon'$ ) and dc conductivity of chitosan and CP blend irradiated with  $C^{+5}$  and  $Ni^{+7}$  ions at fluence of  $1 \times 10^{11}$  and  $1 \times 10^{12}$  ion/cm<sup>2</sup>. The symbols of square and circle referred to chitosan and CP blend, respectively.

properties. In polymeric matrices SHIs induced physicochemical transformation *via* structural rearrangements, chemically changed through macromolecular chains randomization and optical modifications reasonably stimulated in their dielectric responses. Indeed, the orientation of the segmental and side chains highly influenced due to their surroundings event relating to improve nanoscale free volume, degrade polymeric chains, and established conjugation networks. For comparison of MeV ions impact at fluences of  $1 \times 10^{11}$  and  $1 \times 10^{12}$  ions/cm<sup>2</sup> on both the matrices, procured estimations of crystallite size, bandgap, dielectric constant at 1 kHz, and dc conductivity are outlined and shown in [Figure 3.15](#). The XRD analysis revealed that owing to the crystalline domain accredited from PEO, the structural degradation of the CP blend relatively hindered and perceived significant deterioration in crystallite size for chitosan. FESEM strongly supports the XRD relevance and specified that the flattered polymeric surface ascribed to the amorphous phase. The vibration spectra revealed macromolecular structural degradation via branching of main chains with side chains as well as massive hydrogen abstractions. Due to the SHIs effect, newer carbonyl linkage for chitosan observed, while its deficiency observed for CP blend revealed mutual stabilizing effect involving components of both polymers during irradiation. An obsessive hydrogen in association with end groups abstraction yielding C=O, C=C and C=NH chromophores and outgassing of volatile gaseous products as well. Also, the optical data revealed that the diminishing in electronic transition energy owing to defect formation and biodegradable matrices turn to carbon-rich due to  $sp^2$  hybridization aided compact carbon clustering. SHIs induced physicochemical responses inclusively play a persuasive contribution in their respective dielectric characteristics. As revealed from [Figure 3.15](#), at higher fluence the dielectric constant of CP blend relatively found higher than chitosan. The  $M''$  spectra clearly showed that the relaxation and conduction mechanism presumably associated with the physicochemical properties of pre and post irradiated matrices. An increase in charge carriers density boosted dc conductivity. The physicochemical reform also contributes their relevance to fluence and frequency dependant ac conductivity. The  $Ni^{+7}$  ions with higher  $S_e$  compressively revealed remarkable attributes on biodegradable matrices. Noted that the SHIs induced effect also relied on the feature of the matrix itself as well. An outcome of investigation reveals that the accurately preselected beam parameters capable of designing an appropriate biomaterial with desired characteristics, which have their immense significance in diverse disciplines.

## REFERENCES

- [1] G.B. Patel, N.L. Singh, F. Singh, Modification of chitosan-based biodegradable polymer by irradiation with MeV ions for electrolyte applications, *Mater. Sci. Eng. B.* 225 (2017) 150–159. doi:10.1016/j.mseb.2017.08.023.
- [2] S. Wang, L. Shen, W. Zhang, Y. Tong, Preparation and Mechanical Properties of Chitosan/Carbon Nanotubes Composites, *Biomacromolecules.* 6 (2005) 3067–3072. doi:10.1021/bm050378v.
- [3] P. Murugaraj, D.E. Mainwaring, D.C. Tonkin, M. Al Kobaisi, Probing the dynamics of water in chitosan polymer films by dielectric spectroscopy, *J. Appl. Polym. Sci.* 120 (2011) 1307–1315. doi:10.1002/app.33163.
- [4] J. Kowalonek, Surface and thermal behavior of chitosan/poly(ethylene oxide) blends, *Mol. Cryst. Liq. Cryst.* 640 (2016) 78–89. doi:10.1080/15421406.2016.1255518.
- [5] W. Kemp, *Organic Spectroscopy*, Macmillan Education UK, London, 1991. doi:10.1007/978-1-349-15203-2.
- [6] D.K. Avasthi, G.K. Mehta, *Swift Heavy Ions for Materials Engineering and Nanostructuring*, Springer Netherlands, Dordrecht, 2011. doi:10.1007/978-94-007-1229-4.
- [7] G.B. Patel, N.L. Singh, F. Singh, P.K. Kulriya, Effects of MeV ions on physicochemical and dielectric properties of chitosan/PEO polymeric blend, *Nucl. Instruments Methods Phys. Res. Sect. B Beam Interact. with Mater. Atoms.* 447 (2019) 68–78. doi:10.1016/j.nimb.2019.03.052.
- [8] J. Kowalonek, Surface and thermal properties of UV-irradiated chitosan/poly(ethylene oxide) blends, *J. Photochem. Photobiol. A Chem.* 348 (2017) 209–218. doi:10.1016/j.jphotochem.2017.08.035.
- [9] C.A. Daniels, *Polymers: Structure and Properties*, CRC Press, USA, 1989.
- [10] M.H. Abou-Taleb, Characterization of Polymer Blends Using UV-Visible Spectroscopy, in: *Charact. Polym. Blends*, Wiley-VCH Verlag GmbH & Co. KGaA, Weinheim, Germany, 2014: pp. 789–820. doi:10.1002/9783527645602.ch24.
- [11] E.H. Lee, Ion-beam modification of polymeric materials – fundamental principles and applications, *Nucl. Instruments Methods Phys. Res. Sect. B Beam Interact. with Mater. Atoms.* 151 (1999) 29–41. doi:10.1016/S0168-583X(99)00129-9.
- [12] B. Wang, W. Huang, L. Chi, M. Al-Hashimi, T.J. Marks, A. Facchetti, High- $k$  Gate Dielectrics for Emerging Flexible and Stretchable Electronics, *Chem. Rev.* 118 (2018) 5690–5754. doi:10.1021/acs.chemrev.8b00045.
- [13] M.F. Shukur, R. Ithnin, H. a. Illias, M.F.Z. Kadir, Proton conducting polymer electrolyte based on plasticized chitosan–PEO blend and application in electrochemical devices, *Opt. Mater. (Amst).* 35 (2013) 1834–1841. doi:10.1016/j.optmat.2013.03.004.

- [14] R.J. Sengwa, S. Choudhary, Investigation of correlation between dielectric parameters and nanostructures in aqueous solution grown poly(vinyl alcohol)-montmorillonite clay nanocomposites by dielectric relaxation spectroscopy, *Express Polym. Lett.* 4 (2010) 559–569. doi:10.3144/expresspolymlett.2010.70.
- [15] S.B. Aziz, Z.H. Z. Abidin, A. K. Arof, Influence of silver ion reduction on electrical modulus parameters of solid polymer electrolyte based on chitosan-silver triflate electrolyte membrane, *Express Polym. Lett.* 4 (2010) 300–310. doi:10.3144/expresspolymlett.2010.38.
- [16] G.C. Psarras, K.G. Gatos, J. Karger-Kocsis, Dielectric properties of layered silicate-reinforced natural and polyurethane rubber nanocomposites, *J. Appl. Polym. Sci.* 106 (2007) 1405–1411. doi:10.1002/app.26831.
- [17] C.C. Ku, R. Liepins, *Electrical properties of polymers*, Hanser Publishers New York, 1987.
- [18] A.K. Jonscher, *Universal relaxation law: a sequel to Dielectric relaxation in solids*, Chelsea Dielectrics Press, 1996.
- [19] D. Fink, *Fundamentals of Ion-Irradiated Polymers*, Springer Berlin Heidelberg, Berlin, Heidelberg, 2004. doi:10.1007/978-3-662-07326-1.
- [20] K. Ghosal, A. Chandra, P. G., S. S., S. Roy, C. Agatemor, S. Thomas, I. Provaznik, Electrospinning over Solvent Casting: Tuning of Mechanical Properties of Membranes, *Sci. Rep.* 8 (2018) 5058. doi:10.1038/s41598-018-23378-3.
- [21] G.B. Patel, S. Bhavsar, N.L. Singh, F. Singh, P.K. Kulriya, SHI induced modification in structural, optical, dielectric and thermal properties of poly ethylene oxide films, *Nucl. Instruments Methods Phys. Res. Sect. B Beam Interact. with Mater. Atoms.* 379 (2016) 156–161. doi:10.1016/j.nimb.2016.04.018.
- [22] A. Karmakar, A. Ghosh, Poly ethylene oxide (PEO)–LiI polymer electrolytes embedded with CdO nanoparticles, *J. Nanoparticle Res.* 13 (2011) 2989–2996. doi:10.1007/s11051-010-0194-x.